Perfusion Pressure Is a Critical Determinant of the Intratumoral Extravasation of Oncolytic Viruses

Amber Miller[1,2], Rebecca Nace[1], Camilo Ayala-Breton C[1], Michael Steele[1], Kent Bailey[3], Kah Whye Peng[1,4] and Stephen J Russell[1,5]

[1]Department of Molecular Medicine, Mayo Clinic, Rochester, Minnesota, USA; [2]Mayo Graduate School, Center for Clinical and Translational Science, Mayo Clinic, Rochester, Minnesota, USA; [3]Department of Biomedical Statistics and Informatics, Mayo Clinic, Rochester, Minnesota, USA; [4]Department of Obstetrics and Gynecology, Mayo Clinic, Rochester, Minnesota, USA; [5]Division of Hematology, Department of Medicine, Mayo Clinic, Rochester, Minnesota, USA

Antitumor efficacy of oncolytic virotherapy is determined by the density and distribution of infectious centers within the tumor, which may be heavily influenced by the permeability and blood flow in tumor microvessels. Here, we investigated whether systemic perfusion pressure, a key driver of tumor blood flow, could influence the intratumoral extravasation of systemically administered oncolytic vesicular stomatitis virus (VSV) in myeloma tumor-bearing mice. Exercise was used to increase mean arterial pressure, and general anesthesia to decrease it. A recombinant VSV expressing the sodium iodide symporter (NIS), which concentrates radiotracers at sites of infection, was administered intravenously to exercising or anesthetized mice, and nuclear NIS reporter gene imaging was used to noninvasively track the density and spatial distribution of intratumoral infectious centers. Anesthesia resulted in decreased intratumoral infection density, while exercise increased the density and uniformity of infectious centers. Perfusion state also had a significant impact on the antitumor efficacy of the VSV therapy. In conclusion, quantitative dynamic radiohistologic imaging was used to noninvasively interrogate delivery of oncolytic virotherapy, highlighting the critical importance of perfusion pressure as a driver of intratumoral delivery and efficacy of oncolytic viruses.

Received 2 November 2015; accepted 27 November 2015; advance online publication 5 January 2016. doi:10.1038/mt.2015.219

INTRODUCTION

Oncolytic viruses (OV) are experimental cancer therapies quickly approaching approval for clinical use. Numerous viruses from diverse families are being investigated as oncolytic agents.[1] These viruses are naturally evolved or genetically engineered to selectively replicate in and cause damage to cancerous cells while leaving healthy cells unharmed.[2,3] OV can also be genetically enhanced by arming them with therapeutic or reporter transgenes to enhance tumor-cell toxicity or assist researchers in understanding and monitoring virus delivery and replication.[4] OV are used preclinically and in clinical trials to treat multiple types of cancer including hematologic malignancies like multiple myeloma. The treatment of multiple myeloma or similar multifocal, dispersed, or hard to reach cancer deposits requires the use of systemic cancer-tropic OV. Currently, however, the use of systemically administered viruses in clinical trials has resulted in variable delivery in the tumor and limited clinical responses.[5] While there are many genetic strategies to enhance the safety and efficacy of OV, further optimization strategies are needed to address the physical barriers to curative treatment with systemically administered OV.

Vesicular stomatitis virus (VSV) is a tumor-tropic OV due to sensitivity to antiviral effects of interferon (IFN) signaling which is often aberrant in tumor cells but robust in healthy cells.[6] VSV is a negative strand RNA virus of the rhabdoviridae family and has a well understood lifecycle including rapid replication, large burst size, and efficient cytopathic effects.[7–10] VSV is also amenable to genetic manipulation, allowing for further attenuation by deletion of methionine 51 of the matrix (M) protein, VSV-Δ51, which enhances IFN sensitivity and selectivity for IFN defective cancer cells.[11] The VSV genome is also amenable to the insertion of reporter transgenes like the sodium iodide symporter (NIS) gene that when expressed allows tracking of infection. The NIS protein concentrates radioiodide or analogous radiotracers in VSV-NIS infected cells, thereby coupling radiotracer concentration with active viral genome amplification and gene expression.[12–18] The concentration of radiotracers can be detected with nuclear imaging techniques such as single photon emission computed tomography co-registered with X-ray computed tomography (SPECT/CT). The NIS-mediated imaging has been used to monitor intratumoral VSV infection preclinically.[16,19,20]

Nuclear NIS imaging has revealed heterogeneity in the intratumoral density and spatial distribution of VSV-NIS infection centers after systemic virus administration to tumor-bearing mice.[20] Heterogeneous intratumoral infection distribution results in volumes of tumor that remain void of infection. It is hypothesized that these volumes of tumor void of infection are a result of inefficient delivery and extravasation or inability to achieve viremic threshold necessary to establish infection. Such infection voids could contribute to tumor recurrence or lack of tumor clearance. In fact, our mathematical model predicts that OV therapeutic efficacy is directly influenced by the density and distribution

Correspondence: Stephen J. Russell, Department of Molecular Medicine, Mayo Clinic, 200 First Street SW, Rochester, MN 55905, USA. E-mail: sjr@mayo.edu

of intratumoral infection.[21] Therefore, in order to improve on the homogeneity of infection distribution and the efficacy of systemically administered OV, barriers to delivery must be addressed.

Virus delivery to the tumor from the systemic circulation is dependent on rate and distribution of blood flow and the permeability of tumor microvasculature allowing for extravasation across vessel walls. This transvascular transport can be impaired by irregular vascular formation, inadequate tumor perfusion, low vessel permeability, and high interstitial fluid pressure.[5] Tumor vasculature is chaotic in terms of vessel length, diameter, distribution, and blood flow velocity and direction resulting in regions of poor perfusion and low oxygenation that are characteristically difficult to therapeutically target.[22,23] Tumor perfusion and blood flow can be increased for the purpose of therapeutic delivery through physiologic or hemodynamic manipulation of the systemic vasculature. This is because poorly differentiated tumor microvessels do not maintain blood flow volume homeostasis like systemic vasculature. Therefore, an increase in peripheral resistance and blood pressure results in increased blood flow and perfusion pressure in the tumor.[24–28] Indeed, transient small changes in blood flow have been shown to result in changes in hypoxic regions of tumors and improve delivery of chemotherapy and other therapeutic nanoparticles in solid tumors resulting in enhanced survival.[24–30]As OV are nanoparticles, it is hypothesized that similar hemodynamic manipulations, which have yet to be used in combination with OV, may influence intratumoral density and distribution of infection, ultimately resulting in an impact on the clinical outcome of OV.

Until recently, invasive histological techniques were necessary to assess intratumoral infection. Advances in nuclear molecular imaging and reporter gene technologies like NIS now allow quantitative and high resolution observation of intratumoral infectious centers noninvasively.[31] Quantitative analysis of radiotracer concentration has been shown to accurately reflect whole tumor activity and infection burden.[17,18,32,33] NIS mediated imaging has been used to observe intratumoral infection by multiple viruses including adenovirus, herpes simplex virus, measles virus, vaccinia virus, and VSV, and this technology is being translated for clinical monitoring and pharmacokinetic studies. The use of high resolution NIS mediated imaging of OV infection has been labeled "dynamic radiohistology" for its ability to observe the changing temporal and spatial context of intratumoral infectious centers with resolution approaching that of invasive histological techniques.[17,20,34] This provides both qualitative and quantitative assessment of virus delivery which can be used to assist in treatment design and optimization.

The objective of this study was to improve upon the current strategies used to enhance OV efficacy by optimizing intratumoral delivery of systemically administered OV. Since the density and distribution of intratumoral infection by systemically administered OV is hindered by transvascular transport barriers including poor perfusion pressure, hemodynamic manipulations were used to alter intratumoral perfusion pressure. Dynamic radiohistology was then used to quantitatively assess changes in intratumoral infection density and distribution and subsequent therapeutic efficacy of systemically administered VSV as a result of different intratumoral perfusion states.

RESULTS

Heterogeneous delivery has been identified as a barrier to the success of OV.[31] Intratumoral delivery is influenced by both transvascular and interstitial movement of viral particles. It is known that interstitial stromal barriers are minimal in plasmacytomas.[35] Therefore, multiple myeloma tumor models provide a tool for investigating transvascular transport barriers including those related to perfusion, permeability, and irregular vasculature. Here, the aim of this study was to better understand how altering perfusion pressure will affect intratumoral delivery and therapeutic efficacy of systemically administered VSV.

Tumor vasculature

Since tumor vasculature is known to be irregular, it could be hypothesized that a lack of vasculature would result in a lack of virus particle delivery. To ensure vasculature density did not confound the investigation of perfusion pressure, the relationship between vascular density and VSV infection density and distribution was first investigated in 5TGM1 syngeneic multiple myeloma tumors. Tumors were explanted from KaLwRij mice 24 hours after i.v. administration of 2×10^8 $TCID_{50}$ (50% tissue culture infective dose) VSV-GFP. Using immunofluorescent staining of tumor sections against blood vessels (CD31) and VSV infection, the presence of blood vessels, areas of infection, and areas void of infection could be visualized. While the presence of blood vessels is necessary for virus particle delivery to initiate infection, image quantification revealed a higher density of blood vessels did not drive a higher density of intratumoral infection within tumor tissue (**Figure 1**).

Hemodynamic manipulations

Finding no correlation between vascular density and the density of intratumoral infection, it was hypothesized that the cause of heterogeneous intratumoral infection density and distribution could be related to the perfusion state of the tumor vasculature. Since perfusion is dependent on blood pressure, hemodynamic manipulations to increase or decrease systemic mean arterial pressure (MAP) were used to increase or decrease intratumoral perfusion pressure, respectively.

Virus infusion protocols were identified in which hemodynamic manipulations reliably increased or decreased MAP for a sustained period of time during which virus administration was possible. Wireless telemetry devices were used to monitor changes in MAP during hemodynamic manipulations for protocol development. The changes in MAP were reproducible across multiple mice and could be maintained to allow for administration of virus while MAP is elevated or lowered (**Figure 2a**,**b**). Clinically relevant methods of hemodynamic manipulation were used to induce hypertensive and hypotensive conditions. To induce hypertensive, high perfusion conditions, exercise was used. There was an exercise-intensity dependent increase in MAP (data not shown), and a rate of 20 m/minute was chosen for elevating MAP during virus administration. Exercise at a rate of 20 m/minute significantly increased systemic MAP, with a mean increase of 21.51 mm Hg (**Figure 2c**, $P = 0.001$, paired t-test). To induce hypotensive, low perfusion conditions, general anesthesia (isoflurane in O_2) was used. There was an isoflurane dose-dependent

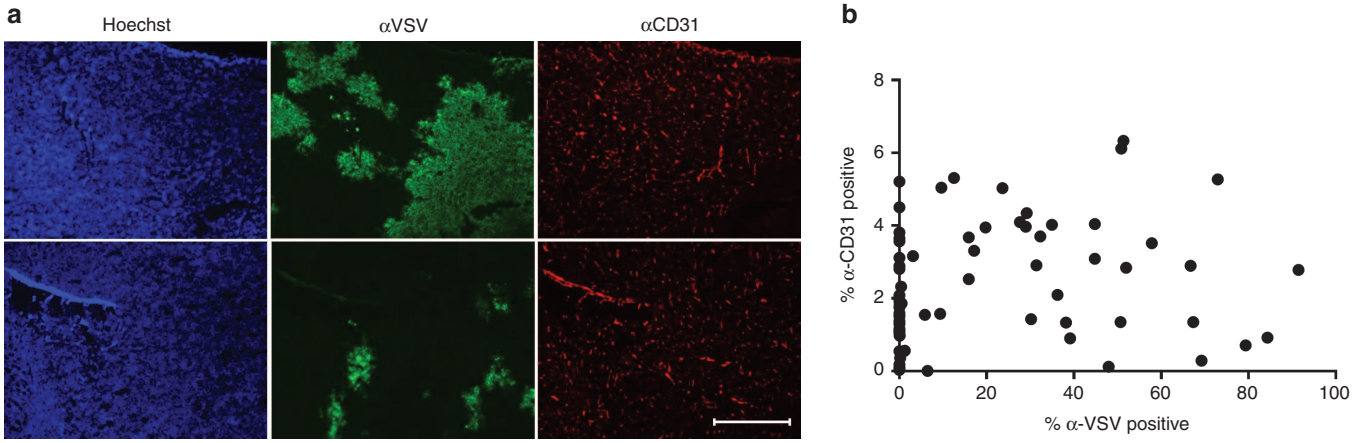

Figure 1 Immunofluorescent staining of tumor vasculature does not correlate with density of VSV-GFP infection. (**a**) Representative immunofluorescent staining of tumor section explanted from 5TGM1-tumor-bearing KaLwRij mice 24 hours post i.v. 2×10^8 $TCID_{50}$ VSV-GFP. The top and bottom rows show the same tumor section stained with Hoechst (blue) to identify cellular nuclei, anti-VSV (green) to identify regions of VSV infection, and anti-CD31 (red) to identify tumor blood vessels. Top row shows a section of tumor with regions of VSV-GFP infection. Bottom row shows a different section of tumor with minimal VSV-GFP infection. Bar = 500 μm, all images are taken at same magnification. (**b**) Image quantification of multiple images from sections of five different 5TGM1 tumors. The total amount of anti-CD31-positive stained pixels and the total amount of anti-VSV-positive stained pixels was standardized against the total amount of Hoechst-positive stained pixels for each image to determine the percent of tumor tissue stained positive for anti-CD31 and anti-VSV respectively.

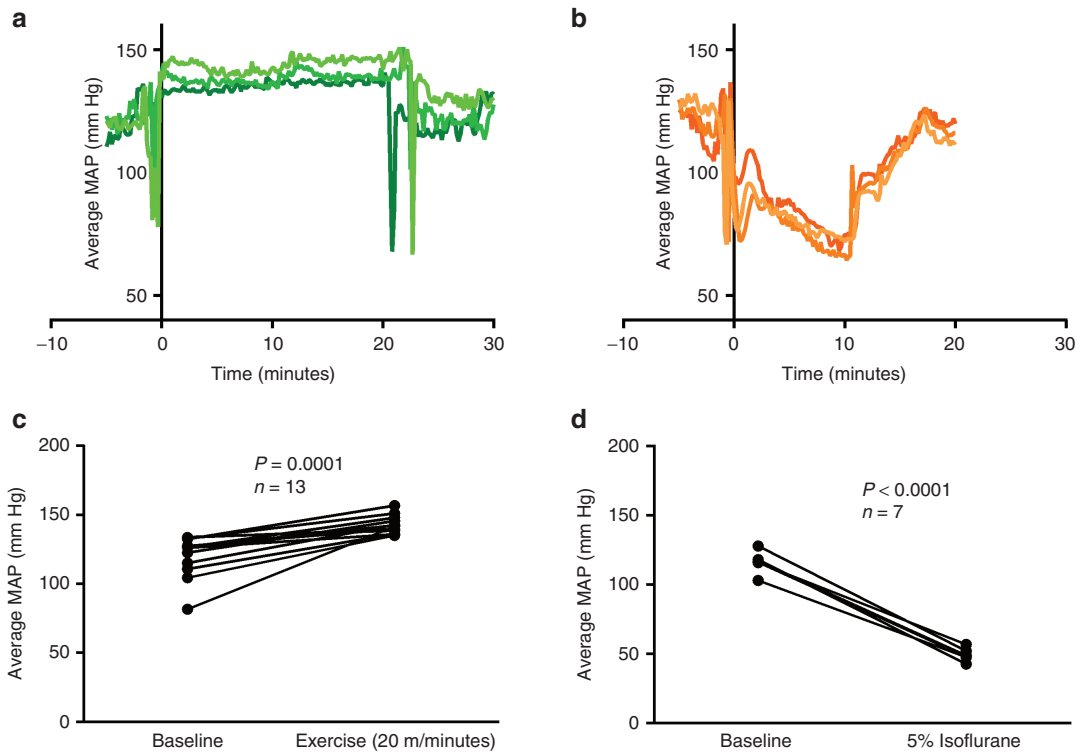

Figure 2 Mean arterial pressure in mice is significantly increased by exercise and significantly decreased by isoflurane. (**a**) Wireless telemetry monitoring of average MAP during the 5 minutes before, 20 minutes during exercise (20 m/minute), and 5 minutes after end of exercise in three separate mice. Large drops in MAP around time 0 minute and 20 minutes are due to movement of mouse on and off treadmill. (**b**) Wireless telemetry monitoring of average MAP during 5 minutes before, 10 minutes during, and 5 minutes after induction with anesthesia (5% isoflurane). Large drops in MAP around time 0 minute and 10 minutes are due to movement of mouse to/from induction chamber. (**c**) Average MAP over 1 minute of exercise 5 minutes prior to exercise compared to the average MAP during 1 minute of exercise after exercising for 10 minutes on the treadmill (20 m/minute) in the same mouse. MAP significantly increases (paired *t*-test, $n = 13$, $P = 0.001$). (**d**) Average MAP (mm Hg) over 1 minute 10 minutes prior to isoflurane induction compared to the average MAP during 1 minute under isoflurane (5%) after 10 minutes of isoflurane induction in the same mouse. MAP significantly decreases (paired *t*-test, $n = 7$, $P < 0.001$).

decrease in MAP (data not shown). The largest decrease in MAP was observed at 5% isoflurane, which significantly decreased systemic MAP with a mean decrease of 67.13 mm Hg (**Figure 2d**, $P < 0.001$, paired *t*-test). This dose was selected for decreasing MAP during virus administration. All mice subsequently treated with hemodynamic manipulations were warmed immediately prior to virus administration to eliminate effects of hemodynamic manipulation-induced changes in body temperature on virus delivery.

Intratumoral delivery and dynamic radiohistology

Virus was administered systemically in temperature-regulated MPC11 syngeneic tumor bearing BALB/C mice during the hemodynamic manipulations described above to determine the effect of altered perfusion pressure on the density and distribution of intratumoral infection. VSV-Δ51-NIS was used to allow visualization of the spatiotemporal changes in intratumoral infection over time via NIS-mediated dynamic radiohistology. Dynamic radiohistology uses nuclear imaging techniques like SPECT/CT to observe concentration of radionuclides in tissues expressing NIS which is coupled to NIS-encoding viral amplification and gene expression. The deletion of methionine 51 attenuates VSV to improve its safety profile. The MPC11 syngeneic tumor model was used because VSV intratumoral infection has been shown previously to spread much more rapidly in this model relative to 5TGM1 tumors, allowing for enhanced early quantitative analysis of SPECT/CT imaging.

In order to effectively compare changes in NIS-mediated radionuclide uptake at centers of infection, a dose-determining study was performed to assess dose- and time-dependent changes in radionuclide concentration (**Supplementary Figure S1**). Consistent with other VSV-NIS dosimetry findings, there is a dose-dependent increase in radionuclide uptake followed by a decrease in radionuclide uptake over time corresponding with cell death after infection.[20] The low dose of 5×10^6 $TCID_{50}$ VSV-Δ51-NIS was chosen so that differences in intratumoral infection density and distribution as a result of altered perfusion pressure could be observed with imaging on days 1–3 (d1–3) following viral administration.

SPECT/CT dynamic radiohistology of syngeneic tumor-bearing mice administered IV VSV-Δ51-NIS during high and low perfusion states allowed visualization of intratumoral infection (**Figure 3** and **Supplementary Figure S2**). Dynamic radiohistology confirmed the persistence of heterogeneous intratumoral infection density and distribution, as seen previously, both within treatment groups and across treatment groups, as evidenced in **Supplementary Figure S2**. Even so, dynamic radiohistology revealed an increase in radiotracer activity, corresponding with infection density, on d1and d2 in mice exercised during virus administration relative to those under anesthesia (**Figure 3** and **Supplementary Figure S2**). Quantitative analysis of radionuclide uptake confirmed a significant increase in uptake intensity per cubic centimeter of tumor in mice exercised during virus administration relative to mice under anesthesia on d1 and d2 (**Figure 3b**, d1 $P = 0.0012$, d2 $P = 0.0064$, unadjusted *t*-test).

Infection distribution

To assess improvements in homogeneity of spatial infection distribution, a novel quantitative method was developed to describe intratumoral distribution patterns (see Materials and Methods and **Figure 4**). During this analysis, high-resolution SPECT/CT imaging data is transformed in order to determine distance to nearest infected neighbor for every point within the tumor volume. This describes the proximity of any given location within the tumor to the closest infectious center. The cumulative distribution of these distances can then be used to describe and compare the distribution pattern of all intratumoral infection. However, every tumor is unique in shape and infection burden such that comparison of the nearest neighbor distances between different tumors is not a useful comparison. For this reason, the distribution of nearest infected neighbor distances for each tumor is compared to that of a theoretically simulated random infection within the same tumor volume for a standardized comparison of deviation from true random distribution. When the cumulative distribution of nearest infected neighbors is plotted for both

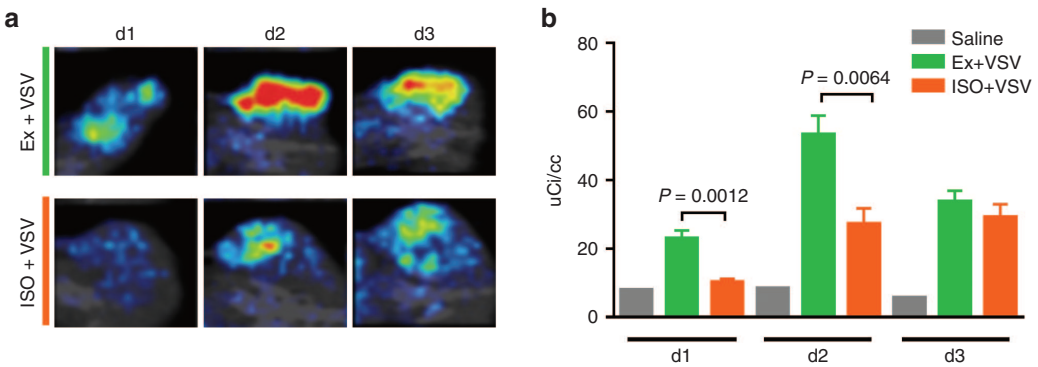

Figure 3 SPECT/CT imaging reveals changes in density and distribution of intratumoral infection centers in animals with altered perfusion states during VSV-Δ51-NIS administration. (**a**) Coronal SPECT/CT planar image through center of representative MPC11 tumor-bearing BALB/C mouse days 1, 2, and 3 following administration of i.v. VSV-Δ51-NIS during exercise (top) or during anesthesia (bottom). (**b**) Quantification of radioactive Tc99m concentration above background per cubic centimeter of tumor in MPC11 tumor bearing BALB/C mice days 1, 2, and 3 following administration of i.v. saline negative control (gray, $n = 1$),VSV-Δ51-NIS during exercise (green, $n = 5$), and VSV-Δ51-NIS during anesthesia (orange, $n = 5$). There is a significant increase in radionuclide uptake in animals exercised during administration of VSV-Δ51-NIS relative to VSV-Δ51-NIS under anesthesia on d1 and d2 (d1 $P = 0.0012$, d2 $P = 0.0064$, *t*-test).

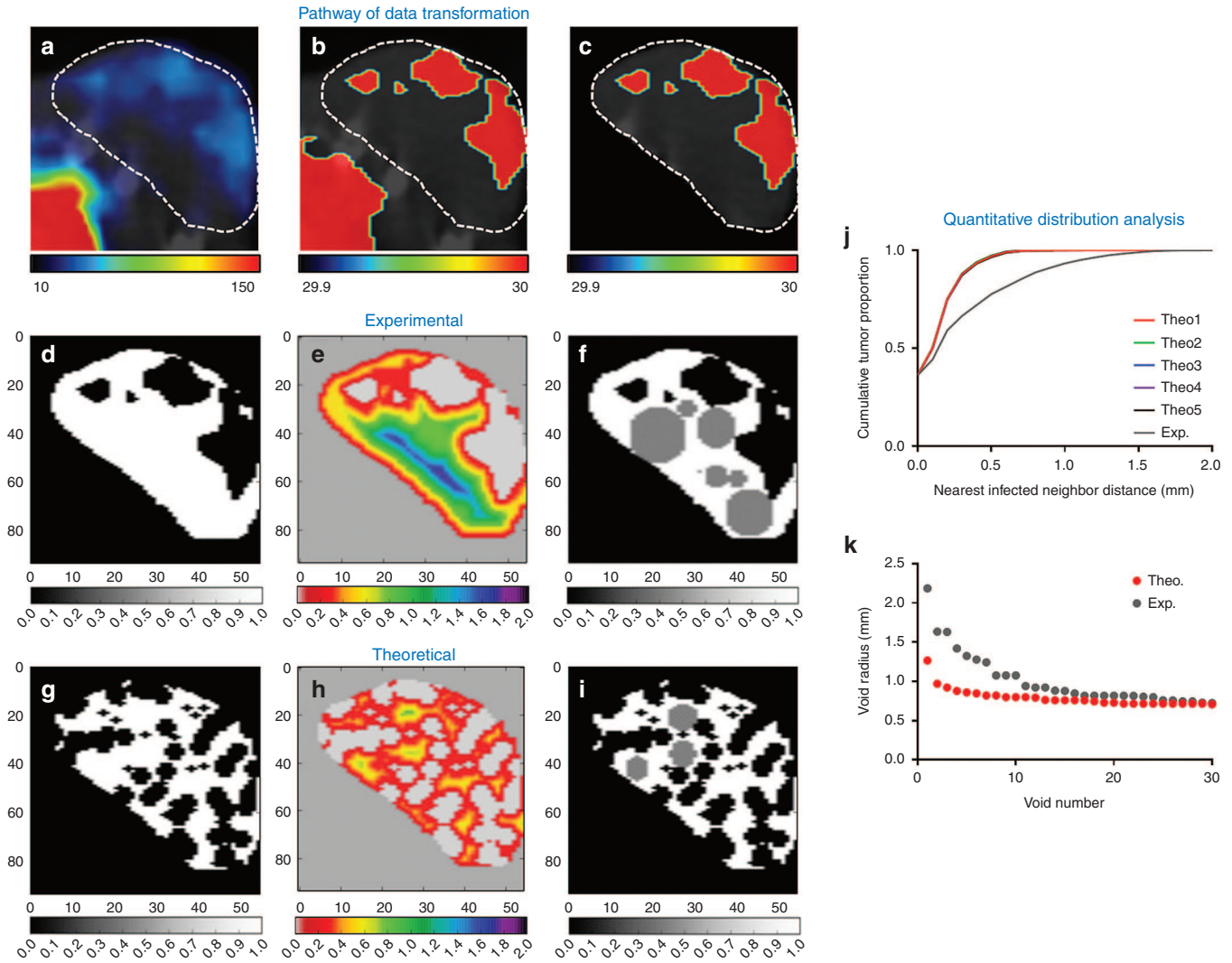

Figure 4 Pathway of data transformation for quantitative distribution and infection void analysis. Data transformation pathway to allow for quantitative distribution analysis by generating binary data labels of infected and uninfected tumor tissue from SPECT/CT images following infection. (**a**) Axial SPCET/CT planar image through representative MPC11 tumor-bearing BALB/C mouse 1d post administration of IV VSV-Δ51-NIS. White dashed outline denotes tumor location. (**b**) Threshold of radiotracer activity is set to distinguish infected from uninfected space. Lower left region of activity is the bladder. (**c**) A label is applied to identify tumor from nontumor space, resulting in (**d**) a binary data set of infected (black within white tumor space) and uninfected tumor tissue (white). (**e**) Distributive distance transformation determines the Euclidean distance to the nearest infected voxel for every voxel within the tumor volume. A heat-map is used to visualize the nearest infected neighbor distances. (**f**) The 30 largest nonoverlapping spherical infection voids are identified from the nearest infected neighbor distances and mapped in gray. (**g**) Theoretical random infection is simulated within the same tumor volume so that the tumor has the same burden of infection as in **d**. (**h**) Distributive distance transformation is performed on theoretical random distribution as in **e**, and (**i**) infection voids are identified as in **f**. (**j**) The cumulative distribution of the nearest neighbor distances describes the distribution of uninfected and infected space and can be used for comparison of distribution to theoretical random distribution. Theo1–Theo5 are the cumulative distributions of five independent theoretical random simulations, demonstrating the repeatability of the random simulation. Exp is the cumulative distribution of the experimentally observed nearest infected neighbor distances. (**k**) The 30 largest nonoverlapping infection voids in experimentally observed (gray) and theoretical random simulated (red) infection distributions can be compared.

experimental and theoretically simulated datasets, the difference in area under the curve (ΔAUC) provides a metric for assessing how similar experimental distribution is to random. The smaller the ΔAUC, the more similar to random and more homogenous the distribution of intratumoral infection is. The nearest infected neighbor distances can also be used to locate the largest spherical, nonoverlapping infection voids that will allow comparison across treatment groups to evaluate whether hemodynamic manipulations affect infection void size.

This distribution analysis was applied to the SPECT/CT imaging of tumor-bearing mice administered IV VSV-Δ51-NIS during high and low perfusion states. Distribution analysis revealed that on average, virus administration during exercise to induce high perfusion pressure resulted in the smallest ΔAUC, resulting in infection distribution that was most similar to theoretically simulated random distribution (**Figure 5**). Virus administered to mice while under anesthesia resulted in the greatest ΔAUC, resulting in infection

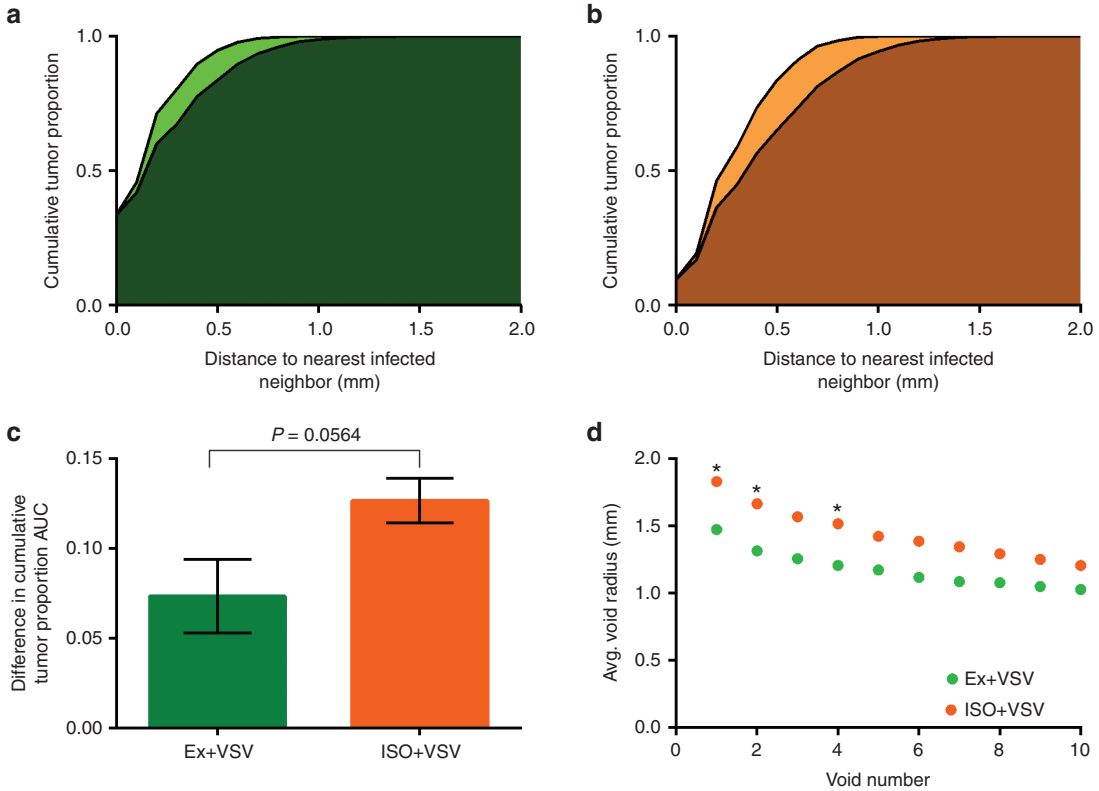

Figure 5 Quantitative distribution analysis shows exercise increases homogeneity of distribution. Average cumulative nearest infected neighbor distance for theoretically simulated random distribution (lighter color) compared to experimentally observed distribution (darker color) for MPC11 tumor-bearing BALB/C mouse 1d post administration of i.v. VSV-Δ51-NIS (**a**) during high perfusion pressure via exercise (green) and (**b**) during low perfusion pressure via isoflurane (orange). Statistical analysis shows the curves are most similar with exercise ($P = 0.0940$) and are statistically different for VSV under isoflurane ($P = 0.0117$). (**c**) Quantification of the mean (±SD) difference in area under the curve (ΔAUC) of cumulative distribution of nearest infected neighbor distances between theoretically simulated random and experimentally observed distributions, indicating magnitude of deviation from random distribution. Virus infusion during exercise resulted in a near significant reduction in ΔAUC relative to isoflurane during infusion ($P = 0.0564$, *t*-test). (**d**) The average radius of the 30 largest, nonoverlapping spherical regions void of infection determined from SPECT/CT imaging d1 after treatment with VSV-Δ51-NIS during exercise ($n = 5$) and VSV-Δ51-NIS during anesthesia ($n = 5$). *Indicates significant difference in average void size ($P < 0.05$, *t*-test).

distribution significantly different than theoretically simulated random distribution (Figure 5, $P = 0.0117$, *t*-test). Moreover, mice administered virus during an induced high perfusion state had increased homogeneity of infection distribution compared to the distribution of infection observed in mice administered virus during low perfusion ($P = 0.0564$, *t*-test). Likewise, mice administered virus during exercise had smaller average infection voids compared to mice administered virus while under anesthesia (Figure 5).

Survival analysis

To determine if the significant change in distribution as a result of perfusion pressure resulted in an effect on therapeutic efficacy, survival analysis was performed on MPC11 tumor-bearing mice treated with i.v. saline control or 5×10^6 $TCID_{50}$ VSV-Δ51-NIS while under high and low perfusion states. Treatment with VSV-Δ51-NIS during high perfusion led to a significant increase in survival relative to mice treated with VSV-Δ51-NIS during low perfusion (Figure 6a, $p = 0.0016$, log-rank (Mantel–Cox) test). Moreover, during low perfusion pressure, VSV-Δ51-NIS treatment provides no significant survival benefit relative to saline (Figure 6a, $P = 0.4629$, log-rank (Mantel–Cox) test).

Similar to the influence of perfusion pressure on survival, there is also a clear difference in disease progression and tumor response as a result of perfusion pressure. Disease progression and cause of death were monitored in all mice following virus administration (**Supplementary Table S1**). It is known that treatment of MPC-11 tumor-bearing mice with VSV-Δ51-NIS causes rapid tumor lysis which can cause toxicity soon after treatment. When response to treatment was assessed in living mice at d11, a time when death was no longer attributed to toxicity, a clear difference in survival benefit was seen. All of the surviving mice treated with VSV-Δ51-NIS during high perfusion pressure were responsive to therapy as monitored by tumor volume (complete response, partial response, or stable disease) while a significantly lower proportion, 33%, of mice treated during low perfusion pressure were responsive to treatment on d11 (Figure 6b, $P = 0.011$, Fischer's exact test). Tracking tumor volume over time showed treatment with IV VSV-Δ51-NIS under high perfusion pressure resulted in greater tumor growth inhibition relative to mice treated under low perfusion pressure (Figure 6c).

Infectious virus recovery was performed to ensure safety and specificity of systemically administered VSV-Δ51-NIS when administered with hemodynamic manipulations. The infectious

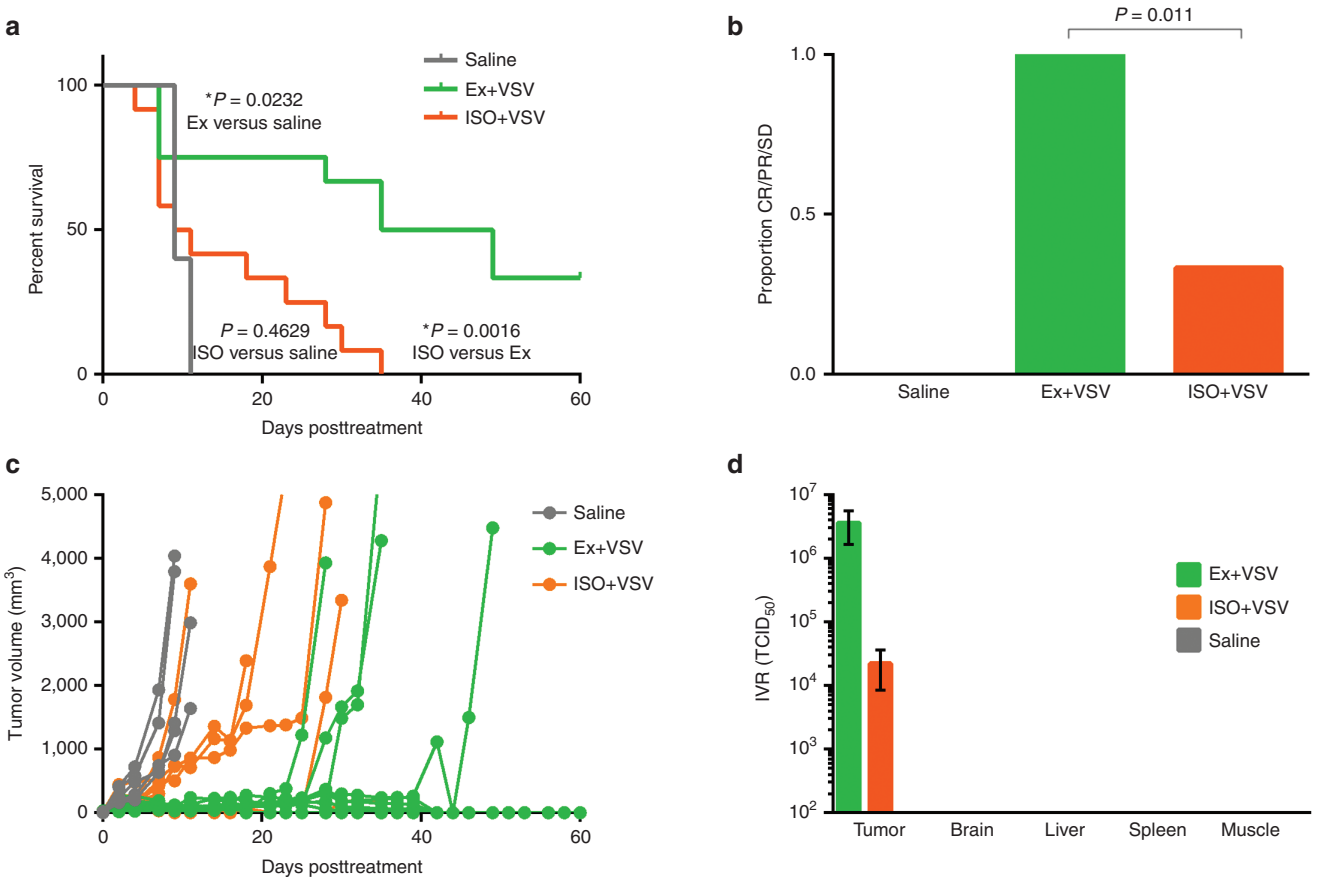

Figure 6 Survival analysis of mice with or without hemodynamic manipulations treated with VSV-Δ51-NIS shows decreased efficacy in hypotensive animals. (**a**) Survival curve following percent of MPC11 tumor bearing BALB/C mice surviving after IV saline control ($n = 5$), VSV-Δ51-NIS during high perfusion (exercise, Ex; $n = 12$), VSV-Δ51-NIS during low perfusion (isoflurane, ISO; $n = 12$). Survival in animals under isoflurane during virus infusion is significantly lower than animals treated during exercise and not significantly different than saline treated animals ($P = 0.0016$, $P = 0.4629$, respectively, Log-rank (Mantel–Cox) test). Survival in animals treated during exercise is significantly higher than saline treated animals ($P = 0.0232$, Log-rank (Mantel–Cox) test). (**b**) Proportion of mice responding (complete response, CR, partial response, PR, or stable disease, SD) to treatment at d11 post virus treatment as determined by tumor volume. Mice treated with virus while under anesthesia have a lower proportion responding to treatment relative to those treated with virus during exercise ($P = 0.011$, Fischer's exact test). (**c**) Tumor growth curves showing tumor size (mm^3) over 60d following for mice treated with i.v. saline (gray), VSV-Δ51-NIS during exercise (green), or VSV-Δ51-NIS during anesthesia (orange). (**d**) Infectious virus recovery from organs harvested 1 day after administration. Limit of detection is 10^2 $TCID_{50}$.

virus recovered from tumors reflects the results of imaging and survival analysis. While there were high titers of infectious virus recovered from tumors harvested from all mice treated with VSV-Δ51-NIS, mice treated under high perfusion pressure had higher titers than those treated under low perfusion pressure (**Figure 6d**). Failure to recover infectious virus above the limit of detection from other organs demonstrates safety and tumor specificity of IV VSV-Δ51-NIS even with altered systemic MAP. Infectious virus recovery was corroborated by similar quantitative real-time polymerase chain reaction of RNA extracted from tumor and tissues (**Supplementary Figure S3**). Furthermore, liver enzyme levels were assessed to address concerns of liver toxicity after infection. In the MPC11 syngeneic-BALB/C model, there was no increase in liver enzyme alanine transaminase and aspartate transaminase levels after treatment with VSV-Δ51-NIS, further confirming safety of this treatment during hemodynamic manipulations (**Supplementary Figure S4**). Elevated enzyme levels are typically detected at higher virus doses and in other models, however. For this reason, liver enzyme levels were measured in 5TGM1-syngeneic tumor-bearing KaLwRij mice treated with i.v. 5×10^7 $TCID_{50}$ VSV-IFNβ-NIS, a similar attenuated VSV, during exercise to ensure that the elevated perfusion pressure did not cause increased liver toxicity. Treatment with VSV-IFNβ-NIS with and without exercise resulted in increased alanine transaminase and aspartate transaminase liver enzyme levels. However, treatment during exercise did not cause additional elevation and may have provided slight protective effects against liver enzyme elevation (**Figure 7**).

DISCUSSION

With the recent US Food and Drug Administration (FDA) approval of the first OV, a genetically modified herpes virus termed Imlygic (talimogene laherparepvec), and because many more OV are approaching clinical trial and FDA approval, there is a continued need to alleviate barriers to success.[36,37] The use of systemic OV is appealing to target distant, difficult to reach, or multiple tumor deposits. However, a distinct barrier to the clinical efficacy of systemic OV is the variability in delivery of

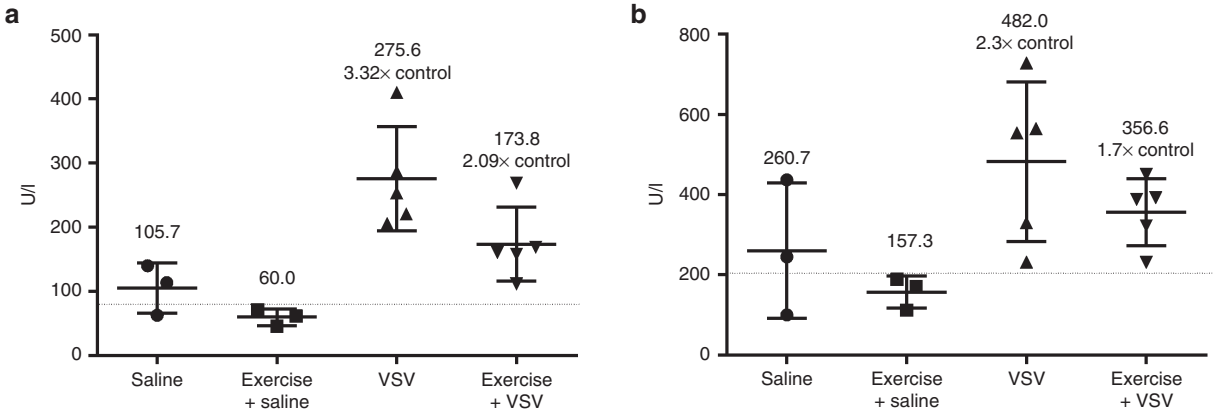

Figure 7 Exercise during intravenous VSV-IFNβ-NIS administration may offer protective effects against liver enzyme elevation in 5TGM1 tumor bearing KaLwRij mice. (**a**) Alanine transferase (ALT) and (**b**) aspartate transferase (AST) liver enzyme levels measured in whole blood from retro orbital eye bleed of 5TGM1 tumor bearing KaLwRij mice 1 day after administration of i.v. saline negative control ($n = 3$), saline during exercise ($n = 3$), $5 \times 10^7 TCID_{50}$ VSV- IFNβ -NIS alone ($n = 5$), and 5×10^7 $TCID_{50}$ VSV- IFNβ -NIS during exercise ($n = 5$). Average levels for each group are labeled and elevation relative to saline control is noted. Reference values for normal enzyme levels, denoted by dashed horizontal line, are subjectively averaged from a variety of sources.

the virus to the tumor site. Moreover, highly variable delivery within tumors of animal models has been shown, with large infectious voids impeding complete tumor clearance. For this reason, we sought to reduce infection voids and improve intratumoral infection distribution by manipulating critical determinants of intratumoral virus extravasation. Here, we were able to show that changes in intratumoral perfusion pressure driven by changes in systemic blood pressure significantly impacted the intratumoral distribution and therapeutic efficacy of systemically administered OV.

By quantifying the density of tumor vasculature and intratumoral infection throughout tumor sections, it was shown that higher tumor vascular density did not drive increased infection density. The low density of vessels in some tissue regions in which infection was detected could be the result of infection-induced vasculature damage. Furthermore, infection voids occurred even in the presence of tumor blood vessels. This alleviates concern that vasculature density varies throughout the tumor or between tumor types, indicating that the inability to initiate infection in tumor voids goes beyond the presence of blood vessels to deliver the virus. Therefore, focus was placed on perfusion pressure since how blood flows through the available vessels may have a greater impact on virus delivery. It has been shown previously that systemic blood pressure is directly related to intratumoral perfusion pressure, and perfusion pressure is necessary for virus extravasation from the vessel into the tumor parenchyma.[22,24,28,38] Changes in perfusion pressure can also impact diffusion coefficients known to be variable or nonexistent in tumors yet important for spread of virus particles throughout the tumor.[39–41]

In order to thoroughly analyze the impact of perfusion pressure on the density and spatial distribution of intratumoral infection, a method for quantitatively comparing distribution patterns was necessary. With advancements in imaging technologies, dynamic radiohistology now provides the means to image intratumoral infection distribution.[20] It is now possible to distinguish the distribution of infectious centers with very high-resolution small animal SPECT/CT imaging instruments like the U-SPECT II (MI Labs, The Netherlands).[34] The detailed three-dimensional (3D) high resolution images are able to be quantitatively analyzed. The novel distribution analysis technique described here allows changes in distribution pattern to be objectively and quantitatively described. Since infectious centers are known to conflate and coalesce, making it impossible to determine the origination of merged infectious centers, a related metric, the nearest infected neighbor distance was used to describe distribution.

The cumulative distribution of nearest infected neighbor distances is useful in describing how far away any location within the tumor is from infection. For instance, the cumulative distribution of nearest neighbor distances can identify when 50% (or 75 or 90%, etc.) of the tumor is within a given distance to infection. This can be thought of as the additional distance that infection would need to spread to infect 50% of the tumor. If the distance is very small, then infection is more homogenously distributed. If the distance is very large, then infection is more clustered with large infection voids. These nearest infected neighbor distances can also be used to compare distribution patterns across treatment groups.

To circumvent the confounding variability in tumor shape, size, and infection burden—as determined by multiple factors including tumor-specific barriers to delivery—it was concluded that the distribution of infection within each tumor should be compared to simulated theoretical random distribution within the same tumor rather than directly compared to the distribution of infection within other tumors that differ in these confounding factors. This provides a standardized and more appropriate comparison. By comparing the observed cumulative distribution of nearest neighbor distances to that of theoretically simulated random infection using ΔAUC, how similar or dissimilar the observed distance to nearest infection is from random for every tumor can be determined; the smaller the ΔAUC, the more similar to random distribution the experimental distribution. In this way, ΔAUC can be used as a nonbiased metric to compare distribution across multiple tumors and across multiple treatment groups. This method of distribution analysis is helpful in not only providing

a means to compare changes in distribution pattern but also in helping to guide future optimizations in virus spread and delivery.

The hemodynamic manipulations were chosen to demonstrate two extreme states of perfusion pressure and selected to replicate scenarios feasible in the clinic. Exercise is frequently used in the clinic during cardiac exercise stress tests. While high-intensity exercise may not be possible for all cancer patients, some physical activity in patients could allow for the small increase in blood pressure seen in mice here. Exercise was also chosen because of the other favorable physiological effects associated with acute exercise including increased rate of blood flow and decreased splanchnic circulation which could protect the liver and spleen from virus particle deposition. The high perfusion pressure as a result of exercise during virus administration resulted in a significant increase in intratumoral infection density and more homogenous infection distribution. This increase was met with a significant increase in survival relative to that achieved with virus administered during a low perfusion pressure state. Anesthesia was used to induce low perfusion pressure because patients routinely undergo anesthesia for procedures, and similar physiologic conditions could also be achieved during periods of rest, immobility, lethargy, coma, or otherwise reduced systemic blood pressure. Anesthesia also lowers core body temperature and slows blood flow, especially to the surface, which may also contribute to a decrease in viral delivery. For this reason, animals from all treatment groups were warmed during virus administration to ensure that body temperature was constant at time of injection. Systemic administration of VSV during the low perfusion state induced by anesthesia resulted in a decrease in density and distribution of intratumoral infection that corresponded with a significant reduction in survival benefit relative to administration during high perfusion. Therefore, the delivery and subsequent efficacy of systemically administered OV is critically dependent on the perfusion pressure driven by systemic blood pressure during infusion.

The clinical implications of this finding should be emphasized, such that patients receiving systemic OV or other targeted cancer therapeutics are kept in an alert state or at the very least avoid hypotensive conditions to allow for the best intratumoral delivery and therapeutic response. Pharmacologic means of increasing or decreasing blood pressure, such as epinephrine or phenylephrine to increase or dobutamine to decrease, are also available. Improvements in intratumoral virus delivery due to epinephrine and phenylephrine were seen when used in preliminary studies (data not shown). It should be noted that different hemodynamic manipulations with similar effects on blood pressure could have different effects on delivery and distribution due to differing mechanisms of action. Pharmacologic means to alter hemodynamics and perfusion pressure could be used to alter delivery in the clinic but will require independent validation.

The increase in intratumoral extravasation, density, and distribution of infection shown here as a result of increased systemic pressure allows hypotheses regarding the underlying mechanisms of delivery to be made that will merit continued investigation. One hypothesis supported by this work is that uneven tumor perfusion may result from differences in interstitial fluid pressure. High interstitial fluid pressure can occlude tumor vasculature, reducing blood flow and access to the tumor. Increased systemic pressure is likely to equilibrate the pressure differential between tumor vasculature and interstitial fluid pressure that would allow for an increase in functional vessels allowing virus to more effectively access the tumor. Similarly, changes in MAP could affect hypoxic tumor regions known to be barriers to intratumoral infection, thereby influencing the density and distribution of infection. It should also be noted that changes in perfusion pressure induced by hemodynamic manipulations were not measured directly but rather indirectly monitored via changes in MAP. While the changes in intratumoral infection density and distribution are assumed to be a result of differences in perfusion pressure, the hemodynamic manipulations used here cause additional physiological effects that could also influence intratumoral delivery. For example, along with a decrease in systemic MAP, isoflurane causes peripheral vascular collapse that could also restrict virus access to the tumor. While perfusion pressure was identified as a critical determinant of intratumoral extravasation here, it will be beneficial to isolate the effects of the different physiological phenomenon underlying the applied hemodynamic manipulations in future experiments to better understand how changes in perfusion pressure mediate changes virus delivery.

It is also worth discussing that a reduction in systemic blood pressure has the potential to reduce intratumoral perfusion pressure and subsequent intratumoral virus extravasation to a greater extent than elevating systemic blood pressure can increase perfusion pressure and virus extravasation. This is because tumor perfusion is dependent on multiple factors including the pressure gradient across the tumor vessel which is determined by both systemic blood pressure and intratumoral interstitial fluid pressure. Other factors including vascular geometry, permeability, resistance to blood flow, and tumor location can also affect tumor perfusion such that the tumor is protected from elevated perfusion pressure.[42] The dependence of tumor perfusion on the systemic to interstitial pressure gradient and vasculature resistance to blood flow will influence the response of tumors to hemodynamic or other vasoactive manipulations.[42] Even so, while it may be difficult to overcome all of these barriers to delivery with a sufficient increase in systemic blood pressure, a reduction in blood pressure will only magnify the intensity of these barriers to intratumoral delivery.

The use of quantitative dynamic radiohistology offers a method for guided therapeutic optimization such as improving distribution of intratumoral infection here. The quantitative imaging data can also help to inform predictive mathematical model development and improvement. There are few inductive mathematical models describing OV currently available, as many are theoretically derived models based on predictions of how virus is delivered, spreads, and interacts with the tumor environment.[21,43–56] The 3D data provided from imaging provides opportunity for more inductive models to be developed that will in turn help describe and understand the dynamic nature of OV that is actually observed. For, example, our previous simplistic mathematical model predicts that therapeutic efficacy is dependent on delivery, which is clearly evidenced here.[21] Furthermore, the model predicts that a sharp therapeutic threshold separates tumor survival from tumor cure which can be bridged by small changes in density or spread of infection centers. This threshold is evident

here where a substantial change in efficacy is seen as a result of a small difference in infection density and uniformity of infection distribution. The 3D data from dynamic radiohistology can also offer a glimpse into the spatial and temporal heterogeneity of infection with capabilities for noninvasive and real-time analysis that have yet to be adequately modeled. The use of dynamic radiohistology to identify infection voids and cumulative nearest infected neighbor distances can provide useful insight to adjust or inform model parameters to improve predictive and inductive modeling.

As the use of systemic OV continues to grow, so does the need to identify and overcome remaining barriers to therapeutic success. Intratumoral perfusion pressure has been identified as a critical determinant of systemically administered OV therapeutic success. Elevation of perfusion pressure has been identified as a clinically relevant means of overcoming barriers to intratumoral transvascular delivery and improving therapeutic efficacy. Using elevated systemic blood pressure to induce elevated perfusion pressure during virus administration resulted in a significant increase in density of infection and improvement in the homogeneity of infection distribution within the tumor. Moreover, the reduction in delivery and significantly heterogeneous distribution due to decreased perfusion pressure during virus administration ultimately resulted in a significant reduction in therapeutic efficacy. This highlights the role that hemodynamics play in driving intratumoral delivery and shows that changes in intratumoral infection density and distribution identified using quantitative dynamic radiohistology have the potential to impact survival. This work identifies the need to focus beyond genetic manipulations of the virus, as manipulations of the host and tumor environment will also impact efficacy of the oncolytic. Based on the evidence here, it is clear that systemic perfusion pressure, a key driver of tumor blood flow, influences the intratumoral extravasation of systemically administered OV and has a critical impact on therapeutic efficacy.

MATERIALS AND METHODS

Cell lines and virus manufacture. Vero cells were obtained from American Type Cell Culture (ATCC, Manassas, VA) and cultured in Dulbecco's Modified Eagles Medium. 5TGM1 murine myeloma cells were obtained from Dr Babatunde Oyajobi (UT Health Sciences Center, San Antonio, TX, originally established from the parent murine 5T33 ($IgG_{2b}\kappa$) myeloma[57]) and cultured in Iscove's Modified Dulbecco's Medium. MPC11 murine myeloma cells were obtained from ATCC and cultured in Dulbecco's Modified Eagles Medium. All cell line culture media was supplemented with 10% serum (fetal bovine serum, for Vero and 5TGM1, horse serum for MPC11), 100 U/ml penicillin and 100 mg/ml streptomycin. 5TGM1 cells are syngeneic to the C57Bl6/KaLwRij mouse strain and MPC11 cells are syngeneic to BALB/C mouse strain. Successful tumor growth in the respective strains confirms cell line identity. These cell lines were not otherwise authenticated.

In vivo studies were performed to evaluate efficacy and distribution of intratumoral infection using various recombinant VSV vectors.

VSV-mIFNβ-NIS, a recombinant VSV containing transgenes coding for murine interferon-β (IFNβ) and the human sodium iodide symporter (NIS) was produced by Mayo Clinic Viral Vector Production Lab (VVPL, Rochester, MN) as described previously.[16]

VSV-GFP, a recombinant VSV containing the transgene coding for green fluorescent protein (GFP), was generated by inserting the cDNA of the GFP gene at engineered restriction sites within the M/G gene junction of the pVSV-XN2 plasmid containing the positive strand antigenome.

VSV-Δ51-NIS, containing a deletion in methionine 51 in the matrix (M) protein and containing the transgene coding for NIS, was generated as described previously.[19]

Virus was rescued and amplified using previously described methods.[16,58] Viral titer was quantified by measuring $TCID_{50}$ on Vero cells calculated using the Spearman–Karber equation as previously described.[59] Virus was stored at −80 °C until use.

Ethics statement. All animals were maintained and cared for in accordance with the Institutional Animal Care and Use Committee of Mayo Clinic (A25514).

Blood pressure monitoring. Wireless telemetry devices (PA-C10 model, Data Sciences International (DSI, St. Paul, MN)) were used to wirelessly and continuously monitor the physiologic parameters in KaLwRij mice. To measure blood pressure, the telemetry system uses a fluid-filled catheter that is inserted into the carotid artery to allow direct and continuous measurements of arterial pressure as it is transduced through the fluid. The catheter is connected to a capsule containing a manometer, battery, signal transmitter, and related electronic hardware that is implanted intraperitoneally by DSI surgeons in anesthetized mice. The pressure wave signals detected at the manometer are converted to radio waves that can be wirelessly transmitted and received by a signal receiver placed externally of the animal's housing. The signal is converted and stored in a digital recorder. Physiological parameters are measured continuously and averaged for every 10 seconds of monitoring. Data acquisition and analysis was performed using DataQuestA.R.T. software (DSI). Animals were allowed 1 week recovery from surgery before measuring blood pressure. Telemetry devices were not implanted in BALB/C mice because a characteristic of the strain is an incomplete circle of Willis, which could result in death after insertion of the catheter into the carotid artery.

Hemodynamic manipulations. Mice implanted with wireless telemetry devices were used to develop the hemodynamic manipulation protocol. Blood pressure changes were determined to be reliable and replicable so that once the protocol was determined, surgical implantation of telemetry devices to monitor hemodynamic changes was not necessary for the remaining survival and distribution experiments. In mice with implanted telemetry devices, blood pressure was manipulated once a day, and measured in up to three separate animals daily to determine protocol. Blood pressure was first monitored during rest for baseline measurements. Blood pressure was then measured in mice for 10 minutes prior to hemodynamic manipulation, throughout the course of hemodynamic manipulation, and until blood pressure returned to resting baseline measurements after hemodynamic manipulation was ceased.

Hemodynamic manipulations applied to mice include exercise on a treadmill (up to 20 m/minute) for 20 minutes to elicit a hypertensive, high perfusion state. Prior to monitoring physiological parameters in exercised mice, mice were first acclimated to and trained on the treadmill for 1 week using increasing pace and duration as described previously.[60] Mice are motivated to run by an electric shock grid that is activated when the animal steps off the treadmill. The shock grid delivers a mild noxious stimulus of 10 V. Exercise is terminated when the animal remains on the shock grid for longer than 5 seconds. To elicit hypotensive conditions and a low perfusion state, anesthetic induction with isoflurane (up to 5% in O_2) for 10 minutes was used.

The determined protocol for hemodynamic manipulation to be followed during virus infusion was as follows: for infusion of virus during high perfusion state, mice were run on a treadmill at 20 m/minute for 10 minutes. Mice were removed and promptly restrained and warmed under a heating lamp for i.v. injection of virus. After injection, mice were placed on the treadmill for an additional 10 minutes of running at a pace of 20 m/minute. For infusion during low perfusion state, mice were

anesthetized with 5% isoflurane for 5 minutes. After 5 minutes, while maintaining anesthesia, the mice were warmed with a heating lamp for i.v. virus infection. After injection, heat was removed and mice remained anesthetized for an additional 5 minutes.

In vivo *studies assessing efficacy and safety of VSV.* 5TGM1 syngeneic murine myeloma tumors were established in mice by subcutaneously implanting 5×10^6 washed 5TGM1 murine myeloma cells (suspended in 100 µl sterile phosphate-buffered saline) in the right flank of ~6-week-old female syngeneic C57Bl6/KaLwRij mice (Harlan, Horst, The Netherlands). MPC11 syngeneic murine myeloma tumors were established in mice by subcutaneously implanting 5×10^6 washed MPC11 murine myeloma cells (suspended in 100 µl sterile phosphate-buffered saline) in the right flank of ~6-week-old female syngeneic BALB/C mice (Harlan, Indianapolis, IN).

When tumors measured ~0.5 cm in diameter, mice were injected with a single i.v. dose of either 100 µl sterile saline or recombinant VSV at a dose up to 2×10^8 $TCID_{50}$. Prior to injection, virus was diluted in sterile saline for a total injection volume of 100 µl per mouse. For infusion during altered perfusion state, mice were administered viral dose as described above.

For survival studies, tumor response was monitored by serial caliper measurements in two dimensions. Tumor volume was calculated using the formula $V = 0.5a^2b$ (where $a \leq b$). Mice were euthanized if tumors reached greater than 10% of mouse body weight, tumors were severely ulcerated, weight loss was greater than 20%, mice were unable to access food and water, or were in obvious distress. Tumor volume was used to determine therapeutic response. Progressive disease was defined as an increase in tumor volume relative to baseline at day 11 posttreatment relative to tumor volume at baseline.

For safety studies, a randomly selected subset of animals treated with recombinant VSV under high and low perfusion states or saline control were euthanized, and blood, tumor, liver, spleen, kidney, brain, and muscle were harvested 24 hours after infection. Blood was stored in lithium heparin microtainer tubes for blood chemistry assays to assess liver enzyme levels. For blood chemistry assays, whole blood was analyzed on a Piccolo Xpress chemistry analyzer with a comprehensive metabolic panel profile (Abaxis, Union City, CA).

Organs were cut into equal sections for storage in RNA*later* stabilization solution (Ambion, Inc., Austin, TX) for RNA extraction and flash frozen in liquid N_2 for infectious virus recovery.

RNA extraction was performed using RNeasy Plus Universal extraction kit. VSV-N and genome copy numbers were quantified using the Roche LightCycler480 quantitative real time polymerase chain reaction Thermocycler using the previously validated and described protocol (Roche, Indianapolis, IN).[61]

Tissue frozen for infectious virus recovery was homogenized and suspended in Opti-MEM buffer. Tissue homogenate was then frozen and thawed twice and centrifuged to separate cellular debris. Supernatant was tittered as described above to quantify any infectious virus recovered from the frozen tissue.

Immunohistochemistry tumor vasculature analysis. Immunohistochemistry analysis of tumor vasculature via anti-CD31 staining was performed on sections from 5TGM1 tumors implanted in syngeneic mice as previously described. Mice were treated with a single i.v. dose of 2×10^8 $TCID_{50}$ VSV-GFP. Tumors from treated mice were harvested 24 hours postinfection and frozen in optimal cutting medium for sectioning. Tumor sections were subject to immunofluorescence staining for (i) VSV antigens using a primary rabbit polyclonal antibody generated by the Mayo Clinic VVPL followed by an Alexa-labeled anti-rabbit secondary antibody (Invitrogen, Molecular Probes), (ii) blood vessels using a primary rat-anti-mouse CD31 polyclonal antibody (BD Pharmingen) followed by an Alexa-labeled anti-rat secondary antibody (Invitrogen), and (iii) cellular nuclei using Hoechst 33342 (Invitrogen). Stained tissue sections were mounted using ProLong Gold Antifade Mountant (Thermo Fischer Scientific, Grand Island, NY). Fluorescent microscopy was used to capture images of the entire tumor tissue section using automatic mosaic tiling performed on the Axiovert 200M Apotome (Zeiss, Göttingen, Germany). ImageJ (NIH) was used to quantify the percent of VSV-positive (green) and CD31-positive (red) pixels within Hoechst positive (blue) tumor tissue.

Nuclear imaging. SPECT/CT imaging was used to visualize concentration of $^{99m}TcO_4^-$ at sites of functional NIS expression coupled to endogenous expression or active viral infection as described previously.[20] Briefly, a dose of 0.5 mCi $^{99m}TcO_4^-$ was administered i.p. to animals 1 hour prior to imaging, and mice were imaged for 25 minutes (5 minutes CT and 20 minutes SPECT) using a high-resolution co-registered microSPECT/CT system (U-SPECT-II, MI labs, Utrecht, The Netherlands) daily on d1–3 post virus administration. Mice were maintained under general anesthesia (isoflurane) during imaging. The images were calibrated using a conversion factor as to allow for quantification of uptake activity in volumes of interest. The NIFTI image flies (.nii) were analyzed using PMOD 3.5 software (PMOD Technologies, Zurich, Switzerland).

Distribution analysis. Data transformation and distribution analysis of SPECT/CT imaging data was performed using custom code written with Python programming language on the Enthought Canopy platform (Enthought, Austin, TX). The process of data transformation and distribution analysis is detailed in **Figure 1**. During this data transformation and analysis technique, the SPECT/CT imaging of intratumoral infection is first transformed to a binary data set distinguishing infected from uninfected tumor tissue by applying a user-defined threshold of radioactivity for positive infection and a CT-guided label of the tumor volume (**Figure 4a–d**). A distributive distance transformation is applied to the binary data set to identify the shortest Euclidean distance from every voxel within the tumor to the nearest "infected" voxel. This identifies the distance to the nearest infected neighbor for every voxel within the tumor image and is used to describe the proximity of any location within the tumor to the closest infectious center (**Figure 4e**). To compare the nearest infected neighbor distance from the observed experimental data, theoretical random infection is simulated within each tumor volume to include the same number of infected cells or voxels. Infection spread is simulated from centers selected using a random number generator. Infection is spread radially outward to cover a sphere surrounding each center with a radius that is defined based on the experimentally observed spread in that tumor. The distributive distance is then performed for the theoretical random distribution (**Figure 4g,h**). The cumulative distribution of nearest infected neighbors is plotted for both experimental and theoretically simulated datasets. A comparison of the difference in area under the curve (ΔAUC) is used as a metric for assessing how similar experimental distribution is to random (**Figure 4j**). The nearest infected neighbor distances are also used to find the largest nonoverlapping spherical infection voids to compare size of uninfected volumes of tumor (**Figure 4f, i, k**).

Quantitative and statistical analysis. All statistical comparisons of tumor growth, treatment response, and differences in distribution observed in BALB/C mice bearing MPC11 tumors after single administration of i.v. VSV-Δ51-NIS at doses of 5×10^6 $TCID_{50}$ during high and low perfusion states compared to saline-treated mice were performed using Prism (GraphPad Software, La Jolla, CA).

SUPPLEMENTARY MATERIAL

Figure S1. VSV-Δ51-NIS dose determination using dosimetry analysis of radionuclide uptake in tumors following virus administration.
Figure S2. Serial SPECT/CT imaging of radionuclide uptake in animals with hemodynamic manipulations during VSV-Δ51-NIS administration.
Figure S3. VSV-N copy numbers in tumor and organs of mice following VSV-Δ51-NIS administration with or without hemodynamic manipulations.
Figure S4. Liver enzyme levels are not elevated after intravenous administration of low dose VSV-Δ51-NIS in mice during hemodynamic manipulations.

Table S1. Cause of death for MPC11 tumor bearing mice treated with IV saline control or VSV-Δ51-NIS during high perfusion (Exercise, Ex) and low perfusion (isoflurane, ISO) states.

ACKNOWLEDGMENTS

A.M. is the Mayo Clinic Gary and Anita Klesch Predoctoral fellow and is supported by Gary and Anita Klesch and Mayo CCaTS Grant Number UL1TR000135 from the National Center for Advancing Translational Sciences. This work was also supported by Al and Mary Agnes McQuinn. S.J.R., K.W.P., and Mayo Clinic have an interest in the NIS reporter gene technology. The technology has been licensed to Imanis Life Sciences. S.J.R., K.W.P., and Mayo Clinic own shares in Imanis Life Sciences.

REFERENCES

1. Donnelly, OG, Errington-Mais, F, Prestwich, R, Harrington, K, Pandha, H, Vile, R *et al.* (2012). Recent clinical experience with oncolytic viruses. *Curr Pharm Biotechnol* **13**: 1834–1841.
2. Russell, SJ, Peng, KW and Bell, JC (2012). Oncolytic virotherapy. *Nat Biotechnol* **30**: 658–670.
3. Russell, SJ and Peng, KW (2007). Viruses as anticancer drugs. *Trends Pharmacol Sci* **28**: 326–333.
4. Cattaneo, R, Miest, T, Shashkova, EV and Barry, MA (2008). Reprogrammed viruses as cancer therapeutics: targeted, armed and shielded. *Nat Rev Microbiol* **6**: 529–540.
5. Miller, A, Russell, SJ (2014). Heterogeneous delivery is a barrier to the translational advancement of oncolytic virotherapy for treating solid tumors. *Virus Adapt Treat* **6**: 11–31.
6. Naik, S and Russell, SJ (2009). Engineering oncolytic viruses to exploit tumor specific defects in innate immune signaling pathways. *Expert Opin Biol Ther* **9**: 1163–1176.
7. Barber, GN (2004). Vesicular stomatitis virus as an oncolytic vector. *Viral Immunol* **17**: 516–527.
8. Kopecky, SA, Willingham, MC and Lyles, DS (2001). Matrix protein and another viral component contribute to induction of apoptosis in cells infected with vesicular stomatitis virus. *J Virol* **75**: 12169–12181.
9. Lichty, BD, Power, AT, Stojdl, DF and Bell, JC (2004). Vesicular stomatitis virus: re-inventing the bullet. *Trends Mol Med* **10**: 210–216.
10. Novella, IS, Ball, LA and Wertz, GW (2004). Fitness analyses of vesicular stomatitis strains with rearranged genomes reveal replicative disadvantages. *J Virol* **78**: 9837–9841.
11. Stojdl, DF, Lichty, BD, tenOever, BR, Paterson, JM, Power, AT, Knowles, S *et al.* (2003). VSV strains with defects in their ability to shutdown innate immunity are potent systemic anti-cancer agents. *Cancer Cell* **4**: 263–275.
12. Barton, KN, Tyson, D, Stricker, H, Lew, YS, Heisey, G, Koul, S *et al.* (2003). GENIS: gene expression of sodium iodide symporter for noninvasive imaging of gene therapy vectors and quantification of gene expression in vivo. *Mol Ther* **8**: 508–518.
13. Dingli, D, Peng, KW, Harvey, ME, Greipp, PR, O'Connor, MK, Cattaneo, R *et al.* (2004). Image-guided radiovirotherapy for multiple myeloma using a recombinant measles virus expressing the thyroidal sodium iodide symporter. *Blood* **103**: 1641–1646.
14. Merron, A, Peerlinck, I, Martin-Duque, P, Burnet, J, Quintanilla, M, Mather, S *et al.* (2007). SPECT/CT imaging of oncolytic adenovirus propagation in tumours *in vivo* using the Na/I symporter as a reporter gene. *Gene Ther* **14**: 1731–1738.
15. Cho, JY, Xing, S, Liu, X, Buckwalter, TL, Hwa, L, Sferra, TJ *et al.* (2000). Expression and activity of human Na+/I- symporter in human glioma cells by adenovirus-mediated gene delivery. *Gene Ther* **7**: 740–749.
16. Naik, S, Nace, R, Federspiel, MJ, Barber, GN, Peng, KW and Russell, SJ (2012). Curative one-shot systemic virotherapy in murine myeloma. *Leukemia* **26**: 1870–1878.
17. Penheiter, AR, Griesmann, GE, Federspiel, MJ, Dingli, D, Russell, SJ and Carlson, SK (2012). Pinhole micro-SPECT/CT for noninvasive monitoring and quantitation of oncolytic virus dispersion and percent infection in solid tumors. *Gene Ther* **19**: 279–287.
18. Groot-Wassink, T, Aboagye, EO, Wang, Y, Lemoine, NR, Reader, AJ and Vassaux, G (2004). Quantitative imaging of Na/I symporter transgene expression using positron emission tomography in the living animal. *Mol Ther* **9**: 436–442.
19. Goel, A, Carlson, SK, Classic, KL, Greiner, S, Naik, S, Power, AT *et al.* (2007). Radioiodide imaging and radiovirotherapy of multiple myeloma using VSV(Delta51)-NIS, an attenuated vesicular stomatitis virus encoding the sodium iodide symporter gene. *Blood* **110**: 2342–2350.
20. Miller, A, Suksanpaisan, L, Naik, S, Nace, R, Federspiel, M, Peng, KW *et al.* (2014). Reporter gene imaging identifies intratumoral infection voids as a critical barrier to systemic oncolytic virus efficacy. *Mol Ther* **1**: 14005.
21. Bailey, K, Kirk, A, Naik, S, Nace, R, Steele, MB, Suksanpaisan, L *et al.* (2013). Mathematical model for radial expansion and conflation of intratumoral infectious centers predicts curative oncolytic virotherapy parameters. *PLoS One* **8**: e73759.
22. Jain, RK (1988). Determinants of tumor blood flow: a review. *Cancer Res* **48**: 2641–2658.
23. Jain, RK (2013). Normalizing tumor microenvironment to treat cancer: bench to bedside to biomarkers. *J Clin Oncol* **31**: 2205–2218.
24. Nagamitsu, A, Greish, K and Maeda, H (2009). Elevating blood pressure as a strategy to increase tumor-targeted delivery of macromolecular drug SMANCS: cases of advanced solid tumors. *Jpn J Clin Oncol* **39**: 756–766.
25. Hattori, Y, Ubukata, H, Kawano, K and Maitani, Y (2011). Angiotensin II-induced hypertension enhanced therapeutic efficacy of liposomal doxorubicin in tumor-bearing mice. *Int J Pharm* **403**: 178–184.
26. Suzuki, M, Hori, K, Abe, I, Saito, S and Sato, H (1981). A new approach to cancer chemotherapy: selective enhancement of tumor blood flow with angiotensin II. *J Natl Cancer Inst* **67**: 663–669.
27. Li, CJ, Miyamoto, Y, Kojima, Y and Maeda, H (1993). Augmentation of tumour delivery of macromolecular drugs with reduced bone marrow delivery by elevating blood pressure. *Br J Cancer* **67**: 975–980.
28. Tozer, GM and Shaffi, KM (1993). Modification of tumour blood flow using the hypertensive agent, angiotensin II. *Br J Cancer* **67**: 981–988.
29. Cárdenas-Navia, LI, Mace, D, Richardson, RA, Wilson, DF, Shan, S and Dewhirst, MW (2008). The pervasive presence of fluctuating oxygenation in tumors. *Cancer Res* **68**: 5812–5819.
30. Maeda, H, Nakamura, H and Fang, J (2013). The EPR effect for macromolecular drug delivery to solid tumors: improvement of tumor uptake, lowering of systemic toxicity, and distinct tumor imaging in vivo. *Adv Drug Deliv Rev* **65**: 71–79.
31. Miller, A, and Russell, SJ (2015). The use of the NIS reporter gene for optimizing oncolytic virotherapy. *Expert Opin Biol Ther*: 1–18.
32. Carlson, SK, Classic, KL, Hadac, EM, Bender, CE, Kemp, BJ, Lowe, VJ *et al.* (2006). *In vivo* quantitation of intratumoral radioisotope uptake using micro-single photon emission computed tomography/computed tomography. *Mol Imaging Biol* **8**: 324–332.
33. Cheng, D, Wang, Y, Liu, X, Pretorius, PH, Liang, M, Rusckowski, M *et al.* (2010). Comparison of 18F PET and 99mTc SPECT imaging in phantoms and in tumored mice. *Bioconjug Chem* **21**: 1565–1570.
34. Ivashchenko, O, van der Have, F, Villena, JL, Groen, HC, Ramakers, RM, Weinans, HH *et al.* (2014). Quarter-millimeter-resolution molecular mouse imaging with U-SPECT$^+$. *Mol Imaging* **13**.
35. Peng, KW, Dogan, A, Vrana, J, Liu, C, Ong, HT, Kumar, S *et al.* (2009). Tumor-associated macrophages infiltrate plasmacytomas and can serve as cell carriers for oncolytic measles virotherapy of disseminated myeloma. *Am J Hematol* **84**: 401–407.
36. FDA (2015). FDA approves first-of-its-kind product for the treatment of melanoma. *FDA News Release*. <http://www.fda.gov/NewsEvents/Newsroom/PressAnnouncements/ucm469571.htm>.
37. Ledford, H (2015). First cancer-fighting virus approved. *Nature* **256**: 622–623.
38. Jain, RK and Stylianopoulos, T (2010). Delivering nanomedicine to solid tumors. *Nat Rev Clin Oncol* **7**: 653–664.
39. Padera, TP, Stoll, BR, Tooredman, JB, Capen, D, di Tomaso, E and Jain, RK (2004). Pathology: cancer cells compress intratumour vessels. *Nature* **427**: 695.
40. Carlisle, R and Coussios, CC (2013). Mechanical approaches to oncological drug delivery. *Ther Deliv* **4**: 1213–1215.
41. Yun, CO (2008). Overcoming the extracellular matrix barrier to improve intratumoral spread and therapeutic potential of oncolytic virotherapy. *Curr Opin Mol Ther* **10**: 356–361.
42. Sensky, PL, Prise, VE, Tozer, GM, Shaffi, KM and Hirst, DG (1993). Resistance to flow through tissue-isolated transplanted rat tumours located in two different sites. *Br J Cancer* **67**: 1337–1341.
43. Dingli, D, Cascino, MD, Josić, K, Russell, SJ and Bajzer, Z (2006). Mathematical modeling of cancer radiovirotherapy. *Math Biosci* **199**: 55–78.
44. Dingli, D, Offord, C, Myers, R, Peng, KW, Carr, TW, Josic, K *et al.* (2009). Dynamics of multiple myeloma tumor therapy with a recombinant measles virus. *Cancer Gene Ther* **16**: 873–882.
45. Paiva, LR, Binny, C, Ferreira, SC Jr and Martins, ML (2009). A multiscale mathematical model for oncolytic virotherapy. *Cancer Res* **69**: 1205–1211.
46. Bajzer, Z, Carr, T, Josić, K, Russell, SJ and Dingli, D (2008). Modeling of cancer virotherapy with recombinant measles viruses. *J Theor Biol* **252**: 109–122.
47. Wein, LM, Wu, JT and Kirn, DH (2003). Validation and analysis of a mathematical model of a replication-competent oncolytic virus for cancer treatment: implications for virus design and delivery. *Cancer Res* **63**: 1317–1324.
48. Wodarz, D, Hofacre, A, Lau, JW, Sun, Z, Fan, H and Komarova, NL (2012). Complex spatial dynamics of oncolytic viruses *in vitro*: mathematical and experimental approaches. *PLoS Comput Biol* **8**: e1002547.
49. Wodarz, D and Komarova, N (2009). Towards predictive computational models of oncolytic virus therapy: basis for experimental validation and model selection. *PLoS One* **4**: e4271.
50. Biesecker, M, Kimn, JH, Lu, H, Dingli, D and Bajzer, Z (2010). Optimization of virotherapy for cancer. *Bull Math Biol* **72**: 469–489.
51. Eftimie, R, Dushoff, J, Bridle, BW, Bramson, JL and Earn, DJ (2011). Multi-stability and multi-instability phenomena in a mathematical model of tumor-immune-virus interactions. *Bull Math Biol* **73**: 2932–2961.
52. Komarova, NL and Wodarz, D (2010). ODE models for oncolytic virus dynamics. *J Theor Biol* **263**: 530–543.
53. Paiva, LR, Martins, ML and Ferreira, SC (2011). Questing for an optimal, universal viral agent for oncolytic virotherapy. *Phys Rev E Stat Nonlin Soft Matter Phys* **84**: 041918.
54. Wodarz, D (2001). Viruses as antitumor weapons: defining conditions for tumor remission. *Cancer Res* **61**: 3501–3507.
55. Wodarz, D (2003). Gene therapy for killing p53-negative cancer cells: use of replicating versus nonreplicating agents. *Hum Gene Ther* **14**: 153–159.
56. Wu, JT, Kirn, DH and Wein, LM (2004). Analysis of a three-way race between tumor growth, a replication-competent virus and an immune response. *Bull Math Biol* **66**: 605–625.
57. Radl, J, Croese, JW, Zurcher, C, Van den Enden-Vieveen, MH and de Leeuw, AM (1988). Animal model of human disease. Multiple myeloma. *Am J Pathol* **132**: 593–597.
58. Whelan, SP, Ball, LA, Barr, JN and Wertz, GT (1995). Efficient recovery of infectious vesicular stomatitis virus entirely from cDNA clones. *Proc Natl Acad Sci USA* **92**: 8388–8392.
59. Hadac, EM, Peng, KW, Nakamura, T and Russell, SJ (2004). Reengineering paramyxovirus tropism. *Virology* **329**: 217–225.
60. Handschin, C, Chin, S, Li, P, Liu, F, Maratos-Flier, E, Lebrasseur, NK *et al.* (2007). Skeletal muscle fiber-type switching, exercise intolerance, and myopathy in PGC-1alpha muscle-specific knock-out animals. *J Biol Chem* **282**: 30014–30021.
61. LeBlanc, AK, Naik, S, Galyon, GD, Jenks, N, Steele, M, Peng, KW *et al.* (2013). Safety studies on intravenous administration of oncolytic recombinant vesicular stomatitis virus in purpose-bred beagle dogs. *Hum Gene Ther Clin Dev* **24**: 174–181.